*Limnol. Oceanogr.*, 46(5), 2001, 1130–1140
© 2001, by the American Society of Limnology and Oceanography, Inc.

# Relationships between *Q*-factor and seawater optical properties in a coastal region

*Giuseppe Zibordi and Jean-François Berthon*
Marine Environment Unit of the Space Applications Institute,
Joint Research Centre of the European Union, 21020 Ispra (VA), Italy

*Abstract*

The *Q*-factor—the ratio between upwelling irradiance and upwelling radiance—describes the bidirectional structure of seawater apparent optical properties as a function of geometry and of marine and atmospheric optical characteristics. A 3-yr time series of $Q_n(\lambda)$ measurements—the *Q*-factor determined by nadir radiance—from the North Adriatic Sea coastal waters, has been analyzed. Scatter plots of $Q_n(\lambda)$ versus sun zenith, $\theta_0$, for different intervals of the diffuse attenuation coefficient $K_d(\lambda)$ have shown a consistent exponential trend. In addition, least-squares regressions of $Q_n(\lambda)$ versus $Q_n(490)$ have exhibited determination coefficients $R^2$ that vary from 0.77 to 0.94 in the spectral range between 412 and 555 nm and $R^2 = 0.50$ at 665 nm. To account for these findings, an empirical model for $Q_n(\lambda)$ as a function of $\theta_0$ and $K_d(\lambda_0)$ at the reference wavelength $\lambda_0 = 490$ nm is proposed for North Adriatic coastal waters.

The capability of modeling the radiance distribution in marine water is a basic step toward the development of advanced remote-sensing techniques for the accurate determination of optically significant components dissolved or suspended in seawater. In this framework, efforts have been devoted to the study of the nonisotropic character of the light distribution in seawater, conveniently expressed through the *Q*-factor. The latter, defined as the ratio between the upwelling irradiance $E_u(z,\lambda)$ and radiance $L_u(\theta,\Delta\varphi,z,\lambda)$ at wavelength $\lambda$ (Tyler 1960; Austin 1979), is a function of (1) the measurement geometry (the sun zenith angle $\theta_0$, the viewing angle $\theta$, the azimuth difference $\Delta\varphi$ between the sun and the observation planes, and depth $z$), (2) the seawater inherent optical properties (the absorption coefficient $a$, the scattering coefficient $b$, and the scattering phase function $P_w$), (3) the atmospheric optical properties (the aerosol optical thickness $\tau_a$ and scattering phase function $P_a$), and (4) sea state and cloud cover. Simplifying the formalism by explicitly showing the dependence on the observation geometry and wavelength only, the *Q*-factor, in units of sr, is given by

$$Q(\theta,\Delta\varphi,z,\lambda) = E_u(z,\lambda)/L_u(\theta,\Delta\varphi,z,\lambda). \quad (1)$$

Theoretical studies on $Q(\theta,\Delta\varphi,z,\lambda)$, specifically focused on oceanic water and based on Monte Carlo simulations, have been carried out by Morel and Gentili (1991, 1993, 1996). A related work (Morel et al. 1995) has shown a good agreement between $Q(\theta,\Delta\varphi,z,\lambda)$ values that result from Monte Carlo simulations and from field measurements performed at 450, 500, and 600 nm in Case 1 water off San Diego and in the Lake Pend Oreille. The latter study has shown $Q(\theta,\Delta\varphi,z,\lambda)$ values ranging from ~1 to 5 sr, with $\theta_0$ ranging from 32° to 80°. In addition to the former work, only a few others have presented experimental $Q(\theta,\Delta\varphi,z,\lambda)$ data. Siegel (1984) discussed $Q_n(\lambda)$ field data—$Q(\theta,\Delta\varphi,z,\lambda)$ at $\theta = 0$ and $z = 0^-$—ranging from 3.4 to 6.4 sr for oceanic water, reporting almost no dependence on wavelength in the spectral interval 450–650 nm and a large dependence on $\theta_0$ between 25° and 80°. Siegel empirically modeled the former dependence on $\theta_0$ through

$$Q_n(\lambda) = Q_{90}(\lambda)\, e^{-C\cos\theta_0}, \quad (2)$$

where $Q_{90}(\lambda)$ defines the value of $Q_n(\lambda)$ at $\theta_0 = 90°$ and $C$ is a function of the seawater optical properties (in Siegel's formulation $C \cos \theta_0$ is expressed by $C \sin \gamma_0$ with $\gamma_0$ sun elevation, i.e., $\gamma_0 = 90 - \theta_0$). An almost identical dependence of $Q_n(\lambda)$ on $\theta_0$ has been confirmed by Aas and Hojerslev (1999) in the spectral interval 465–474 nm, with data collected in the Mediterranean Sea.

Recent measurement activities in the framework of the Coastal Atmosphere and Sea Time Series (CoASTS) project (Berthon et al. 2000) have produced a $Q_n(\lambda)$ data set for the North Adriatic Sea coastal waters over a wide range of $\theta_0$ and environmental conditions. In this work, the latter data set is analyzed and discussed in view of proposing an empirical spectral model for $Q_n(\lambda)$ in North Adriatic coastal waters as a function of $\theta_0$ and of the diffuse attenuation coefficient $K_d(\lambda)$.

## Field measurements

Within the CoASTS project, since fall 1995, atmospheric and marine measurements have been collected in the North Adriatic Sea from the Acqua Alta Oceanographic Tower (AAOT) to support calibration and validation activities of ocean color sensors. The measurement site is located 15 km off the Venice Lagoon (45.314°N, 12.508°E) in a frontal re-

*Acknowledgments*

The contribution of John Doyle in the correction of data for tower shading effects, of Davide D'Alimonte in the data analysis, and of Stanford Hooker in supporting the CoASTS project are acknowledged. Part of the data shown in Table 3 were produced by Cristina Targa, Stefania Grossi, and Dirk van der Linde of the CoASTS Team. Acknowledgments are also due to Luigi Alberotanza, Pierluigi Cova, and Alessandro Vianello of the Italian National Research Council and Armando, Narciso, Daniele, and Gianni, crew of the AAOT, for the continuous support provided during the CoASTS measurement campaigns. The authors are grateful to reviewers for their constructive criticism and suggestions that helped in improving the manuscript.

This work has been supported by the European Commission through contract MAS3CT970087 and by NASA through grant NCC5-371.

gion that, according to marine circulation, can be characterized by Case 1 or Case 2 water. By application of the classification scheme proposed by Loisel and Morel (1998), on the basis of the relationship between chlorophyll *a* concentration and the beam attenuation coefficient $c(\lambda)$ at $\lambda = 660$ nm, the Case 1 water occurrence has been 64% for the measurements performed from January 1997 to December 1998 (Berthon pers. comm.).

The description of the CoASTS measurements, extensively presented in Zibordi et al. (pers. comm.) and in Berthon et al. (pers. comm.), is here summarized for

(1) $L_u(z,\lambda)$ taken at nadir [i.e., $L_u(\theta = 0,\Delta\varphi,z,\lambda)$], $E_u(z,\lambda)$, and $E_d(z,\lambda)$—i.e., the only quantities relevant for $Q_n(\lambda)$ computation and its parameterization as a function of $K_d(\lambda)$; and

(2) the inherent optical properties $a(z,\lambda)$ and $c(z,\lambda)$ [where $c(z,\lambda) = a(z,\lambda) + b(z,\lambda)$].

$Q_n(\lambda)$ *and* $K_d(\lambda)$—$L_u(z,\lambda)$, $E_u(z,\lambda)$, and $E_d(z,\lambda)$ profiles have been taken in seven spectral bands 10 nm wide (centered at 412, 443, 490, 510, 555, 665, and 683 nm) with the WiSPER (Wire-Stabilized Profiling Environmental Radiometer) system, installed on a rig moving along two vertical wires fixed between the tower and the sea bottom. The WiSPER radiometers, mounted at the same level, have been deployed at ~7.5 m from the tower legs with a speed of ~0.1 m $s^{-1}$.

The WiSPER measurements analyzed in this work were collected from fall 1995 to fall 1998 by use of two SATLANTIC (Halifax, Canada) radiometers: an OCR-200 for $L_u(z,\lambda)$ and an OCI-200 for $E_u(z,\lambda)$ and $E_d(z,\lambda)$. Each measurement sequence included simultaneous profiles of $L_u(z,\lambda)$ and $E_u(z,\lambda)$, preceded and followed by simultaneous profiles of $L_u(z,\lambda)$ and $E_d(z,\lambda)$. The duplication of simultaneous $L_u(z,\lambda)$ and $E_d(z,\lambda)$ profiles was mainly intended to characterize the stability of the measurement conditions and hence to provide a suitable means of screening out data significantly affected by changes in sky illumination or in seawater optical properties during the execution of the measurement sequence.

$E_u(z,\lambda)$ and $E_d(z,\lambda)$ profiles were both taken with the same OCI-200, looking down and up, respectively. This significantly reduced the effective signal-to-noise ratio (S/N) in $E_u(z,\lambda)$ measurements. In fact, whereas for $E_d(z,\lambda)$ the S/N was always higher than $\sim 10^4$, for $E_u(z,\lambda)$ it ranged from $5 \times 10^2$ to $10^3$ in the spectral region 412–555 nm, and it was $\sim 1.5 \times 10^2$ at 665 nm.

Subsurface $L_u(0^-,\lambda)$ and $E_u(0^-,\lambda)$ values, corrected for the tower shading, self-shading, and bottom perturbation effects, were obtained from the intercept of the least-squares regression fits of $\ln L_u(z,\lambda)$ and of $\ln E_u(z,\lambda)$ with respect to $z$ in a surface depth interval $z_0 < z < z_1$. Depths $z_0$ and $z_1$ were chosen as to satisfy requirements of linear decay of $\ln L_u(z,\lambda)$ and $\ln E_u(z,\lambda)$ as a function of $z$ (where, at the specific measurement site, $0.3 < z_0 < 1$ m and $2.5 < z_1 < 5$ m). The negative slope of the linear regression fit of $\ln E_d(z,\lambda)$ in the depth interval $z_0$–$z_1$ has given the diffuse attenuation coefficient $K_d(\lambda)$ (which is assumed not to be affected by bottom effects nor by self- and tower-shading perturbations taken independent of $z$).

The correction factors for the tower-shading perturbations were obtained from look-up tables (Doyle and Zibordi 1998) resulting from Monte Carlo computations of radiance and irradiance fields at the AAOT site for the specific point where the WiSPER measurements were taken (Zibordi et al. 1999). For each center-wavelength $\lambda$, the correction factors have been indexed by discrete values of (1) $\theta_0$; (2) $a(\lambda)$ from AC-9 measurements or, alternatively (when AC-9 data were not available), from spectrometric absorption measurements of particulate and dissolved organic matter performed on discrete seawater samples (see the following section); (3) seawater single-scattering albedo $\varpi(\lambda) = b(\lambda)/c(\lambda)$, computed from AC-9 data, or, alternatively, estimated by use of $a(\lambda)$ from spectrometric measurements and $b(\lambda) = a(\lambda)\{103R(0^-,\lambda)/[1 - R(0^-,\lambda)]\}$ (Kirk 1994) with $R(0^-,\lambda) = E_u(0^-,\lambda)/E_d(0^-,\lambda)$; and (4) the diffuse over direct irradiance ratio $r(\lambda)$ obtained from measurements of total $E_d(0^+,\lambda)$ and diffuse $E_i(0^+,\lambda)$ above water downward irradiance {i.e., $r(\lambda) = E_i(0^+,\lambda)/[E_d(0^+,\lambda) - E_i(0^+,\lambda)]$} . The tower-shading percentage corrections on the analyzed $Q_n(\lambda)$ have shown average values and SDs ranging from 0.2% ± 0.4% to 0.81% ± 0.9% at 683 and 490 nm, respectively.

The correction factors for the self-shading perturbations were computed with the scheme proposed by Gordon and Ding (1992) and the parameterizations suggested by Zibordi and Ferrari (1995) and Mueller and Austin (1995). The self-shading correction factors have been computed by use of (1) $\theta_0$, (2) $a(\lambda)$, (3) $r(\lambda)$, and (4) the ratio $d$ between the instrument radius and the sensor entrance optics. The self-shading percentage corrections on $Q_n(\lambda)$ have shown average values and SDs ranging from −0.6% ± 0.4% to −2.9% ± 2.1% at 555 and 683 nm, respectively.

The correction factors for the effects due to the bottom (sand and mud at 17 m depth) were estimated with a simple analytical model adapted from Maritorena et al. (1994). Computations have been performed by use of (1) the bottom reflectance $\rho(\lambda) = E_u(z_b,\lambda)/E_d(z_b,\lambda)$ obtained from each profile at depth $z_b$ near the bottom; (2) the mean diffuse attenuation coefficient $\overline{K_d}(\lambda)$ for the depth interval $z_0$–$z_b$; and (3) the subsurface downwelling irradiance $E_d(0^-,\lambda)$ corrected for the tower-shading perturbation. The bottom effects percentage corrections on $Q_n(\lambda)$ have shown average values and SDs <0.01% ± 0.13% [the latter small values indicates that the bottom effects on $E_u(0^-,\lambda)$ and $L_u(0^-,\lambda)$ are very close and cancel out in the ratio $E_u(0^-,\lambda)/L_u(0^-,\lambda)$].

Major sources of uncertainty in $Q_n(\lambda)$ computed from $L_u(0^-,\lambda)$ and $E_u(0^-,\lambda)$ are attributed to (1) uncertainties in the correction of perturbation effects; (2) uncertainties induced in $L_u(0^-,\lambda)$ and $E_u(0^-,\lambda)$ by the surface effects; (3) uncertainties in the absolute calibration of the OCI-200 and OCR-200 radiometers; and (4) uncertainties in the immersion factors applied to $L_u(z,\lambda)$ and $E_u(z,\lambda)$, and, deviations from the ideal cosine response of the $E_u(z,\lambda)$ collectors. The uncertainty in $Q_n(\lambda)$ due to the instrument S/N, is neglected being minimized by the number $n$ of $L_u(z,\lambda)$ and $E_u(z,\lambda)$ values used to compute $\overline{L_u(0^-,\lambda)}$ and $\overline{E_u(0^-,\lambda)}$ (i.e., the uncertainty decreases with $1/\sqrt{n}$, and in the worst case it has been estimated to be <0.1% at 665 nm).

In Table 1, an estimate of the former uncertainties is given at each considered $\lambda$. The percentage uncertainty $\varepsilon$ in $Q_n(\lambda)$, due to uncertainty in the removal of the perturbation effects,

Table 1. Percentage uncertainties induced in $Q_n(\lambda)$ by the uncertainty in the correction of perturbation effects ($\varepsilon$), the uncertainty in subsurface extrapolation of $L_u(0^-,\lambda)$ and $E_u$ $(0^-,\lambda)$ ($\delta$), the uncertainty in absolute calibration of OCR-200 and OCI-200 radiometers ($\zeta$), and the uncertainty induced by uncertainties in the immersion factors of OCR-200 and OCI-200 and in cosine response of OCI-200 ($\eta$), QS is the quadrature sum of uncertainties assumed to be independent and random.

| $\lambda$ (nm) | 412 | 443 | 490 | 510 | 555 | 665 | 683 |
|---|---|---|---|---|---|---|---|
| $\varepsilon$(%) | 0.8 | 0.4 | 0.2 | 0.2 | 0.2 | 1.1 | 1.2 |
| $\delta$(%) | 0.8 | 1.1 | 1.5 | 1.3 | 1.4 | 1.6 | 1.6 |
| $\zeta$(%) | 1.5 | 1.5 | 1.5 | 1.5 | 1.5 | 1.5 | 1.5 |
| $\eta$(%) | 3.0 | 3.0 | 3.0 | 3.0 | 3.0 | 3.0 | 3.0 |
| QS(%) | 3.5 | 3.6 | 3.7 | 3.6 | 3.6 | 3.9 | 3.9 |

has been estimated under the assumption of a tentative uncertainty of ±25% in the maximum statistical correction applied to the $Q_n(\lambda)$ data set for the removal of tower-shading, self-shading, and bottom effects. The values given in Table 1 are equal to one quarter the average percentage absolute corrections added by their SD. The resulting $\varepsilon$ shows values ranging from 0.2% to 1.2%.

The percentage uncertainty $\delta$ in $Q_n(\lambda)$, due to uncertainty in the extrapolation of $L_u(0^-,\lambda)$ and $E_u(0^-,\lambda)$ from $L_u(z,\lambda)$ and $E_u(z,\lambda)$ profiles, has been computed as ±one half the mean unbiased percentage difference (UPD; i.e., the percentage ratio between the absolute difference of two values and their average) of $Q_n(\lambda)$ from sequential profiles taken on clear sky with $\theta_0 \cong 60°$, $K_d(490) \sim 0.06$ m$^{-1}$, and wave height between 0.5 and 1.25 m. The latter extreme conditions, occasionally observed at the AAOT site during the measurement campaigns, have been producing large surface effects and have been assumed to induce some of the largest uncertainties in the extrapolation of $L_u(0^-,\lambda)$ and $E_u(0^-,\lambda)$ through the whole CoASTS data set. The computed values of $\delta$ given in Table 1 show values ranging from 0.8% to 1.6% and exhibit a general increase with wavelength.

The percentage uncertainty $\zeta$ in $Q_n(\lambda)$, due to the absolute calibration uncertainty of the OCR-200 and OCI-200 radiometers, has been estimated to account for the uncertainty induced in the transfer of an irradiance standard (i.e., a NIST traceable 1,000 W FEL lamp) to a radiance standard through a reflectance plaque. In fact, $Q_n(\lambda)$ is only sensitive to the difference between the absolute calibration accuracy in $L_u(z,\lambda)$ and $E_u(z,\lambda)$, provided that both the OCR-200 and OCI-200 radiometers are calibrated with the same lamp. The values of $\zeta$ given in Table 1 are obtained from the uncertainty of the 99% Spectralon reflectance plaque (Labsphere, Sutton) used for the OCR-200 calibration.

Further relevant uncertainties that may induce spectral changes in $Q_n(\lambda)$ are (1) the uncertainty in the cosine response of the OCI-200 and (2) the uncertainty in the immersion factors of the OCR-200 and OCI-200 used for $L_u(z,\lambda)$ and $E_u(z,\lambda)$ measurements. These uncertainties were not determined prior to the experiment described here. However, accounting for studies on underwater radiometers similar to the OCR-200 and OCI-200 (Mueller 1995; Petzold and Austin 1988), the former uncertainties are estimated to be lower than 3%. The quadrature sum of the uncertainties quantified in Table 1 for $Q_n(\lambda)$ exhibits values ranging from 3.5% at 412 nm to 3.9% at 683 nm.

Table 2. Average UPD and SD $\sigma_d(\lambda)$ computed from $K_d(\lambda)$ values obtained from successive $E_d(z,\lambda)$ profiles. $K(\lambda)$ and $\sigma_K(\lambda)$ indicate $K_d(\lambda)$ average and SD for data included in the $Q_n(\lambda)$ data set.

| $\lambda$ (nm) | Average UPD ± $\sigma_d$ (%) | $K \pm \sigma_K$ (m$^{-1}$) |
|---|---|---|
| 412 | 3.1 ± 3.0 | 0.36 ± 0.15 |
| 443 | 3.9 ± 3.8 | 0.29 ± 0.12 |
| 490 | 4.8 ± 4.3 | 0.21 ± 0.09 |
| 510 | 5.2 ± 4.1 | 0.20 ± 0.07 |
| 555 | 5.1 ± 4.1 | 0.19 ± 0.05 |
| 665 | 2.1 ± 1.6 | 0.61 ± 0.07 |
| 683 | 1.9 ± 1.7 | 0.66 ± 0.08 |

To provide sensitivity on accuracy of $K_d(\lambda)$ used in the present study, UPDs between $K_d(\lambda)$ values computed from the successive $E_d(z,\lambda)$ profiles performed in each measurement sequence just before and just after the $L_u(z,\lambda)$ and $E_u(z,\lambda)$ profiles are given in Table 2 with their SDs. Results show UPDs and SD ranging from 2.1% ± 1.6% at 665 nm to 5.2% ± 4.1% at 510 nm. The average $K_d(\lambda)$ values with SDs are also included in Table 2, for completeness.

a($\lambda$) *and* c($\lambda$)—The seawater absorption $a(\lambda)$ and beam attenuation $c(\lambda)$ coefficients were computed from measurements taken in nine bands 10 nm wide, ranging from 412 to 715 nm with a 25-cm–path length AC-9 (WETlabs, Philomath), equipped with a SeaBird 3K pump for water flow. $a(\lambda)$ and $c(\lambda)$ have been obtained adding the pure sea water absorption $a_w(\lambda)$ (Pope and Fry 1997) and beam attenuation $c_w(\lambda)$ coefficients (the latter computed by use of the scattering coefficients $b_w(\lambda)$ given by Buiteveld et al. 1994) to the AC-9 measurements corrected for salinity and temperature effects (WETlabs 2000). The scattering effects on AC-9 absorption measurement have been removed by application of the method proposed by Zaneveld et al. (1994).

Spectral absorption coefficients $a(\lambda)$ have also been computed as the sum of pure sea water $a_w(\lambda)$, particulate matter $a_p(\lambda)$, and dissolved matter $a_{ys}(\lambda)$ absorption coefficients. $a_p(\lambda)$ has been measured for particles retained on 0.7-$\mu$m pore size glass fiber filters, by use of the spectrometric method proposed by Tassan and Ferrari (1995). $a_{ys}(\lambda)$ has been measured for seawater filtrated through a 0.22-$\mu$m cellulose filter, with use of the spectrometric method proposed by Ferrari et al. (1996).

## Data analysis and modeling

The present $Q_n(\lambda)$ data set, from the CoASTS (1995–1998) time series, has been created by use of measurements collected under ''clear sun'' (i.e., with the sun not obstructed by clouds) and under ''almost stable environmental'' conditions. Clear sun conditions have been identified by the threshold of the ratio between above water diffuse and direct irradiance $r(412) \leq 2.0$. Almost stable environmental conditions have been identified by differences <10% in $L_u(0^-,412)/E_d(0^-,412)$ values computed from the duplicate

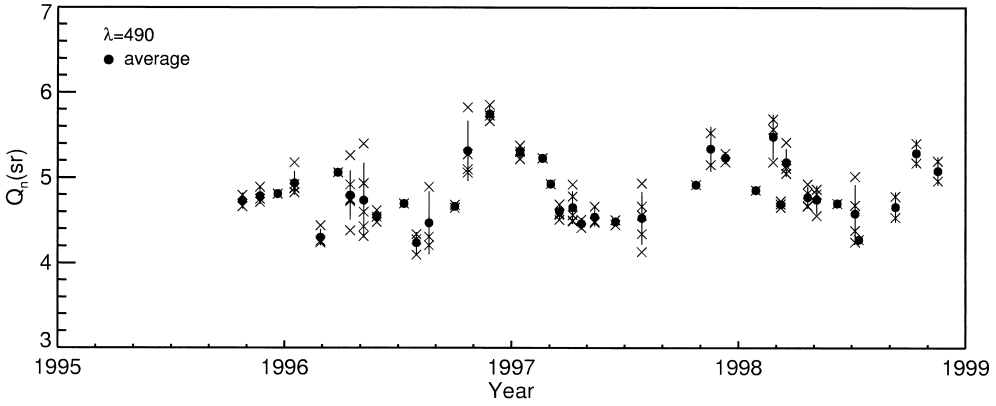


Fig. 1. $Q_n(490)$ from the CoASTS (1995–1998) data set, plotted as a function of time. x, individual data; error bars are SD.

$L_u(z,\lambda)$ and $E_d(z,\lambda)$ profiles performed just before and just after the $L_u(z,\lambda)$ and $E_u(z,\lambda)$ profiles.

Figure 1, which shows the time series of $Q_n(490)$, highlights the existence of well-defined annual cycles. The data display almost regular large variations, which are attributed to changes in the daily maximum sun zenith (in fact, the majority of measurements were performed at a time close to the local noon), overlapped by relatively short-term variations (up to ±10% of the average value) attributed to changes in the seawater optical properties and in the illumination conditions.

The range of variability of the major quantities defining the seawater and atmospheric optical properties for the measurements related to the $Q_n(\lambda)$ data set are given in Table 3. Making use of the selected CoASTS measurements, an empirical modeling of $Q_n(\lambda)$ has been investigated as a function of $\theta_0$ and of different apparent or inherent seawater optical properties [i.e., $K_d(\lambda)$, $a(\lambda)$, $b(\lambda)$, and $\varpi(\lambda)$]. Among the inherent and apparent optical properties, $K_d(\lambda)$ has shown the best correlations for a basic parameterization of $Q_n(\lambda)$. In the following subsections, the $Q_n(\lambda)$ dependence on $\theta_0$ and $K_d(\lambda)$ is presented, whereas elements on $Q_n(\lambda)$ dependence on $a(\lambda)$, $b(\lambda)$, and $\varpi(\lambda)$ will be given in the Discussion section.

*Spectral dependence*—All the $Q_n(\lambda)$ spectra considered in this study are shown in Fig. 2. The corresponding average values are given in Table 4 with their SDs.

Table 3. Range of variability of the major quantities defining the seawater and atmospheric optical properties related to the $Q_n(\lambda)$ data set: Chl *a*, total suspended matter (TSM), beam attenuation coefficient at 676 nm ($c$), particulate matter absorption at 412 nm ($a_p$), dissolved organic matter absorption at 412 nm ($a_{ys}$), and aerosol optical thickness at 555 nm ($\tau_a$).

| | Minimum | Maximum | Average |
|---|---|---|---|
| Chl *a* ($\mu$g $L^{-1}$) | 0.1 | 8.3 | 1.3 |
| TSM (mg $L^{-1}$) | 0.2 | 5.1 | 1.1 |
| $c$ (676) ($m^{-1}$) | 0.2 | 3.8 | 1.0 |
| $a_p$ (412) ($m^{-1}$) | 0.03 | 0.37 | 0.11 |
| $a_{ys}$ (412) ($m^{-1}$) | 0.04 | 0.26 | 0.12 |
| $\tau_a$ (555) | 0.02 | 0.26 | 0.14 |

The $Q_n(\lambda)$ spectra exhibit an appreciable dependence on $\lambda$. On average, they show a slight decrease from 412 to 510 nm and an increase up to 665 nm followed by a decrease at 683 nm. The general decrease in $Q_n(\lambda)$ from 412 to 510 nm does not appear in the simulated spectra proposed for oceanic waters by Morel and Gentili (1996). In fact, the latter $Q_n(\lambda)$ spectra given for $30° < \theta_0 < 75°$ and chlorophyll concentrations ranging from 0.03 to 3 mg $m^{-3}$ show a general increase with $\lambda$ from 412 to 670 nm. The different spectral behavior in the blue can probably be explained by a more pronounced absorption (in particular because of yellow substance and nonpigmented particles), characterizing the present experimental data with respect to the theoretical data set simulated by Morel and Gentili (1996) for Case 1 water. Specifically, in the present study, the seawater absorption coefficients $a(\lambda)$ show an average value of 0.24 ± 0.09 $m^{-1}$ at 412 nm, against the maximum value of 0.04 $m^{-1}$ at 400 nm used by Morel and Gentili (1993). In addition, the present high $Q_n(412)$ values could also be partially explained by a poor estimate of the OCI-200 immersion factor at 412 nm provided by the instrument manufacturer (~5% higher than

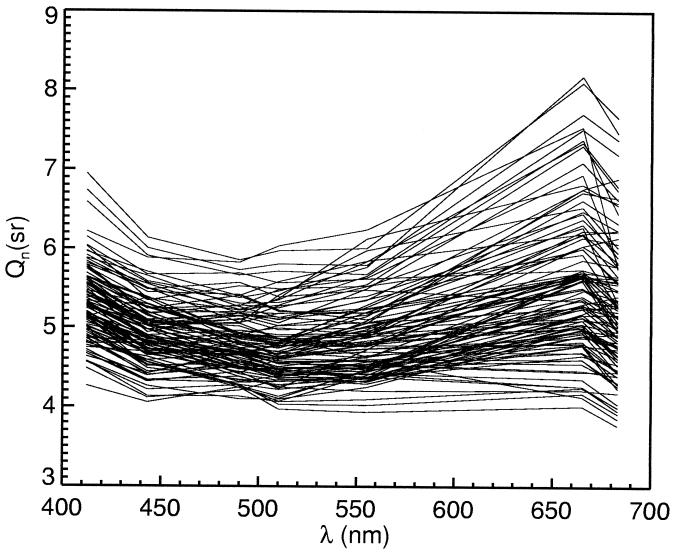


Fig. 2. $Q_n(\lambda)$ spectra from the CoASTS (1995–1998) data set.

Table 4. Average $Q_n(\lambda)$ from the CoASTS (1995–1998) data set and SDs $\sigma_Q(\lambda)$.

| $\lambda$ (nm) | 412 | 443 | 490 | 510 | 555 | 665 | 683 |
|---|---|---|---|---|---|---|---|
| $Q_n \pm \sigma_Q$ (sr) | 5.31 ± 0.47 | 4.94 ± 0.42 | 4.81 ± 0.39 | 4.75 ± 0.43 | 4.87 ± 0.49 | 5.56 ± 0.99 | 5.26 ± 0.83 |

that at the closer wavelengths). The decrease at 683 nm is likely attributed to Chl *a* fluorescence that, acting as a ''source of diffuse light,'' induces a more isotropic light field and hence a decrease in $Q_n(683)$ with respect to $Q_n(665)$. Because of this, in the aim of restricting the discussion on $Q_n(\lambda)$ at wavelengths characterized by elastic scattering only, $Q_n(683)$ is not included in the following analysis.

Figure 3 displays the scatter plots of $Q_n(\lambda)$ versus $Q_n(\lambda_0)$ with $\lambda_0 = 490$ nm and the corresponding linear regression fits obtained according to

$$Q_n(\lambda) = A_0(\lambda) + S(\lambda)Q_n(\lambda_0). \quad (3)$$

The coefficients computed from the regressions are given in Table 5 with their 90% confidence intervals. The regressions at different $\lambda$ reflect the spectral changes in $Q_n(\lambda)$ with respect to $Q_n(490)$ observed in Fig. 2. The scattering of data with respect to the regression line leads to determination coefficients $R^2$ ranging from 0.77 to 0.94 in the spectral range 412–555 nm and $R^2 = 0.50$ at 665 nm. The lower correlation for $Q_n(665)$ is attributed to the lower penetration

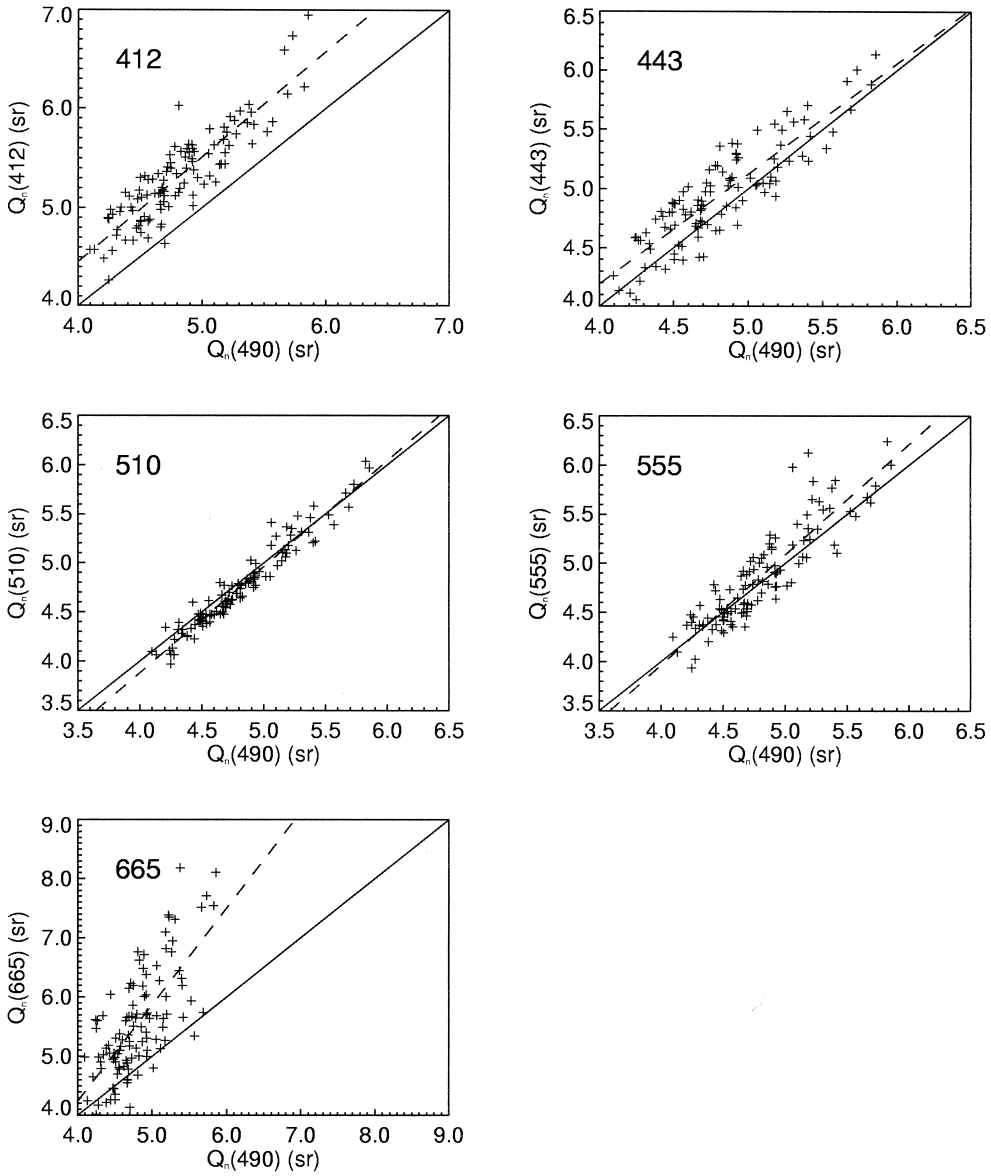


Fig. 3. Scatter plots of $Q_n(\lambda)$ vs. $Q_n(490)$. Dashed lines show the linear regression fits, and the solid lines indicate the 1 : 1 ratio.

Table 5. Coefficients of the linear regression fits of $Q_n(\lambda)$ vs. $Q_n(490)$ computed with use of Eq. 3. Values in parentheses indicate the 90% confidence interval.

| $\lambda$ (nm) | $A_0$ | $S$ | $R^2$ ($n$ = 109) |
|---|---|---|---|
| 412 | 0.197 (0.433) | 1.063 (0.090) | 0.78 |
| 443 | 0.456 (0.394) | 0.934 (0.082) | 0.77 |
| 510 | −0.441 (0.210) | 1.081 (0.043) | 0.94 |
| 555 | −0.533 (0.444) | 1.124 (0.092) | 0.79 |
| 665 | −2.286 (1.246) | 1.631 (0.258) | 0.50 |

depth of light at 665 nm with respect to shorter $\lambda$. Because of this, in the presence of an optical stratification occurring just below the surface, $Q_n(665)$ could exhibit a spectral behavior different from $Q_n(\lambda)$ at shorter $\lambda$ as being related to a ''different'' water volume. Additional uncertainty in $Q_n(665)$ could be induced by fluorescence edge effects in presence of high Chl *a* concentrations.

The use of a $\lambda_0$ different from 490 nm could produce better or worse regressions (as actually produced by $\lambda_0$ = 412 or $\lambda_0$ = 665 nm, respectively), but this would not change the main conclusions of the work. The choice of $\lambda_0$ = 490 nm has here been driven by the need to link $Q_n(\lambda)$ to an operational ocean color product such as $K_d(490)$, to give an applicative view to the study.

*Sun zenith and* $K_d$ *dependence*—Figure 4 shows scatter plots of $Q_n(\lambda)$ as a function of the sun zenith $\theta_0$ at 412, 490, 555, and 665 nm (i.e., at wavelength considered representative for ocean color studies). The general increase of $Q_n(\lambda)$ with $\theta_0$ shows consistency with results proposed by Morel and Gentili (1996) and by Aas and Hojerslev (1999).

To investigate the dependence of $Q_n(\lambda)$ on $\theta_0$ and seawater optical properties, the $Q_n(\lambda)$ data have been distributed into three different classes $i$ = 1–3 defined by intervals of $K_d(\lambda)$ [i.e., $K_d(\lambda,i)$] . The former intervals have been selected as to constitute, for each $\lambda$, three equal logarithmic ranges within the observed $K_d(\lambda)$ span (the number of elements in each interval may change as a function of $\lambda$). The small number of classes has been suggested by the need of differentiating each class through a representative number of elements.

The fitting functions drawn in Fig. 4 for each class $i$ have been computed with

$$Q_n(\lambda,i) = Q_{90}(\lambda,i)\,\exp[-C(\lambda,i)\cos\theta_0]. \quad (4)$$

For each $\lambda$, the $K_d(\lambda,i)$ interval limits and the resulting coefficients $C(\lambda,i)$ and $Q_{90}(\lambda,i)$ with their 90% confidence intervals are given in Table 6. $C(\lambda,i)$ and $Q_{90}(\lambda,i)$ show a general increase with $K_d(\lambda,i)$ values at each $\lambda$. However, the $C(\lambda,i)$ and $Q_{90}(\lambda,i)$ 90% confidence intervals exhibit quite large values because of the scattering of $Q_n(\lambda,i)$ data around the fitting curves. This scattering probably results from (1) surface effects in $E_d(z,\lambda)$ that cause uncertainty in the retrieved $K_d(\lambda)$; (2) the very different environmental conditions (i.e., sky radiance distribution and water type) characterizing the measurements; and (3) the relatively small

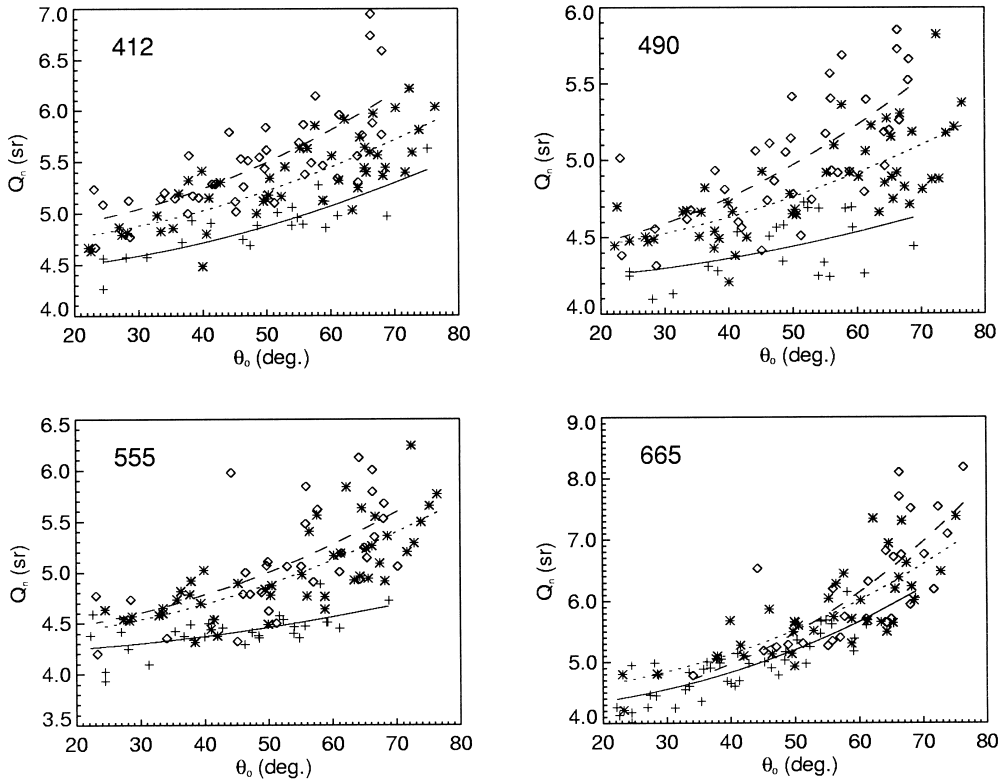


Fig. 4. $Q_n(\lambda,i)$ plotted as a function of $\theta_0$ for the three classes $i$ defined by $K_d(\lambda,i)$ values, with the associated exponential fitting curves at 412, 490, 555, and 665 nm. + and solid lines, class 1; * and dotted lines, class 2; and ◇ and dashed lines, class 3.

Table 6. Coefficients $Q_{90}(\lambda,i)$ and $C(\lambda,i)$ from the exponential fits of $Q_n(\lambda,i)$ vs. $\theta_0$ obtained with Eq. 4 for different classes $i$ defined by the interval limits $K_d$ min and $K_d$ max. $a$, $b$, and $\varpi$ are average subsurface (0.5–4.5m) values (± SD) computed with AC-9 measurements (whose number was generally lower than $n$). PDs are the average absolute percentage differences between $Q_n(\lambda,i)$ and fitted values. Coefficients $Q_{90}(\lambda,i)$ have been computed with constant $C(\lambda)$. Values in parentheses indicate the 90% confidence intervals.

| $\lambda$ (nm) | $i$ | $K_d$min ($m^{-1}$) | $K_d$max ($m^{-1}$) | $n$ | $a \pm \sigma_a$ ($m^{-1}$) | $b \pm \sigma_b$ ($m^{-1}$) | $\varpi \pm \sigma_\varpi$ | $Q_{90}$(sr) | $C$ | $R^2$ | PD (%) | $\bar{Q}_{90}$ (sr) | $\bar{C}$ | PD (%) |
|---|---|---|---|---|---|---|---|---|---|---|---|---|---|---|
| 412 | 1 | 0.107 | 0.206 | 21 | 0.128 ± 0.025 | 0.476 ± 0.157 | 0.783 ± 0.033 | 5.815 (1.598) | 0.274 (0.422) | 0.71 | 2.44 | 5.965 (0.014) | | 2.56 |
| 412 | 2 | 0.206 | 0.352 | 46 | 0.207 ± 0.041 | 0.842 ± 0.270 | 0.796 ± 0.036 | 6.334 (0.858) | 0.301 (0.230) | 0.63 | 3.78 | 6.381 (0.290) | 0.315 | 3.77 |
| 412 | 3 | 0.352 | 0.756 | 42 | 0.340 ± 0.092 | 1.758 ± 0.762 | 0.827 ± 0.041 | 7.042 (1.277) | 0.386 (0.281) | 0.54 | 4.36 | 6.735 (0.310) | | 4.31 |
| 443 | 1 | 0.088 | 0.160 | 18 | 0.099 ± 0.021 | 0.421 ± 0.097 | 0.808 ± 0.033 | 5.396 (1.987) | 0.256 (0.564) | 0.58 | 2.99 | 5.567 (0.471) | | 2.85 |
| 443 | 2 | 0.160 | 0.292 | 50 | 0.168 ± 0.034 | 0.773 ± 0.256 | 0.816 ± 0.032 | 5.887 (0.812) | 0.304 (0.231) | 0.63 | 3.98 | 5.892 (0.277) | 0.305 | 3.98 |
| 443 | 3 | 0.292 | 0.688 | 41 | 0.290 ± 0.090 | 1.741 ± 0.733 | 0.848 ± 0.037 | 6.392 (1.258) | 0.349 (0.306) | 0.54 | 4.06 | 6.220 (0.312) | | 4.18 |
| 490 | 1 | 0.058 | 0.127 | 22 | 0.084 ± 0.021 | 0.492 ± 0.162 | 0.850 ± 0.036 | 4.877 (1.780) | 0.146 (0.544) | 0.24 | 3.40 | 5.275 (0.418) | | 3.57 |
| 490 | 2 | 0.127 | 0.219 | 49 | 0.122 ± 0.020 | 0.815 ± 0.275 | 0.863 ± 0.026 | 5.510 (0.775) | 0.227 (0.230) | 0.54 | 3.38 | 5.635 (0.274) | 0.267 | 3.52 |
| 490 | 3 | 0.219 | 0.500 | 38 | 0.200 ± 0.059 | 1.762 ± 0.740 | 0.891 ± 0.028 | 6.253 (1.317) | 0.357 (0.337) | 0.51 | 4.68 | 5.917 (0.315) | | 4.90 |
| 510 | 1 | 0.074 | 0.131 | 22 | 0.082 ± 0.013 | 0.462 ± 0.181 | 0.838 ± 0.047 | 4.693 (1.760) | 0.128 (0.559) | 0.17 | 3.65 | 5.221 (0.425) | | 3.80 |
| 510 | 2 | 0.131 | 0.211 | 53 | 0.108 ± 0.020 | 0.832 ± 0.266 | 0.880 ± 0.025 | 5.550 (0.769) | 0.251 (0.224) | 0.50 | 3.93 | 5.684 (0.269) | 0.292 | 4.05 |
| 510 | 3 | 0.211 | 0.446 | 34 | 0.172 ± 0.046 | 1.759 ± 0.776 | 0.901 ± 0.036 | 6.304 (1.411) | 0.380 (0.367) | 0.47 | 5.23 | 5.983 (0.335) | | 5.38 |
| 555 | 1 | 0.096 | 0.139 | 30 | 0.103 ± 0.014 | 0.544 ± 0.165 | 0.832 ± 0.042 | 4.948 (1.598) | 0.162 (0.453) | 0.35 | 2.61 | 5.748 (0.391) | | 3.95 |
| 555 | 2 | 0.139 | 0.202 | 47 | 0.114 ± 0.011 | 0.912 ± 0.341 | 0.878 ± 0.039 | 6.040 (0.862) | 0.331 (0.240) | 0.60 | 4.06 | 6.204 (0.298) | 0.379 | 4.39 |
| 555 | 3 | 0.202 | 0.376 | 32 | 0.145 ± 0.022 | 1.830 ± 0.764 | 0.918 ± 0.026 | 6.353 (0.711) | 0.372 (0.192) | 0.38 | 6.05 | 6.376 (0.361) | | 6.05 |
| 665 | 1 | 0.477 | 0.571 | 44 | 0.338 ± 0.011 | 0.671 ± 0.282 | 0.639 ± 0.099 | 7.618 (1.913) | 0.594 (0.345) | 0.73 | 4.44 | 8.474 (0.425) | | 4.54 |
| 665 | 2 | 0.571 | 0.657 | 38 | 0.344 ± 0.009 | 1.026 ± 0.537 | 0.711 ± 0.107 | 8.077 (1.283) | 0.592 (0.282) | 0.63 | 5.70 | 8.759 (0.402) | 0.744 | 6.45 |
| 665 | 3 | 0.657 | 0.819 | 27 | 0.363 ± 0.017 | 1.809 ± 0.852 | 0.807 ± 0.070 | 9.168 (1.573) | 0.803 (0.363) | 0.56 | 7.77 | 8.929 (0.449) | | 7.96 |

Table 7. Coefficients $C$ ($\lambda$,$i$) and $Q_{90}$($\lambda$,$i$) from the exponential fits of $Q_n$($\lambda$,$i$) vs. $\theta_0$ obtained with Eq. 4 for different classes $i$ defined by the interval limits $\varpi$ min and $\varpi$ max. Values in parentheses indicate the 90% confidence intervals. PDs are the average absolute percentage differences between $Q_n$($\lambda$,$i$) and fitted values.

| $\lambda$ (nm) | $i$ | $\varpi$ min | $\varpi$ max | $n$ | $Q_{90}$ (sr) | $C$ | $R^2$ | PD (%) |
|---|---|---|---|---|---|---|---|---|
| 412 | 1 | 0.710 | 0.788 | 20 | 6.512 (1.436) | 0.365 (0.342) | 0.72 | 3.89 |
| 412 | 2 | 0.788 | 0.822 | 19 | 6.512 (1.436) | 0.202 (0.464) | 0.37 | 3.78 |
| 412 | 3 | 0.822 | 0.913 | 20 | 6.728 (2.643) | 0.357 (0.574) | 0.33 | 5.24 |
| 443 | 1 | 0.745 | 0.807 | 17 | 6.061 (1.423) | 0.365 (0.378) | 0.79 | 3.40 |
| 443 | 2 | 0.807 | 0.836 | 19 | 5.591 (2.181) | 0.210 (0.574) | 0.22 | 4.58 |
| 443 | 3 | 0.836 | 0.932 | 23 | 6.068 (2.404) | 0.313 (0.553) | 0.33 | 4.65 |
| 490 | 1 | 0.788 | 0.860 | 25 | 5.807 (1.293) | 0.302 (0.354) | 0.71 | 3.03 |
| 490 | 2 | 0.860 | 0.883 | 15 | 6.054 (2.986) | 0.340 (0.702) | 0.26 | 6.19 |
| 490 | 3 | 0.883 | 0.955 | 19 | 6.207 (2.586) | 0.350 (0.580) | 0.46 | 3.81 |
| 510 | 1 | 0.743 | 0.863 | 16 | 5.918 (0.016) | 0.385 (0.005) | 0.76 | 3.25 |
| 510 | 2 | 0.863 | 0.910 | 32 | 5.815 (1.563) | 0.308 (0.375) | 0.47 | 4.11 |
| 510 | 3 | 0.910 | 0.960 | 11 | 6.733 (4.552) | 0.471 (1.069) | 0.35 | 4.80 |
| 555 | 1 | 0.771 | 0.866 | 20 | 6.504 (1.753) | 0.515 (0.441) | 0.68 | 4.67 |
| 555 | 2 | 0.866 | 0.912 | 26 | 6.076 (1.787) | 0.348 (0.412) | 0.49 | 4.32 |
| 555 | 3 | 0.912 | 0.961 | 13 | 7.248 (3.261) | 0.588 (0.675) | 0.53 | 6.19 |
| 665 | 1 | 0.365 | 0.543 | 18 | 8.951 (2.186) | 0.849 (0.423) | 0.73 | 5.82 |
| 665 | 2 | 0.543 | 0.672 | 25 | 7.494 (1.983) | 0.578 (0.371) | 0.80 | 3.91 |
| 665 | 3 | 0.672 | 0.831 | 16 | 8.701 (3.704) | 0.736 (0.640) | 0.79 | 3.68 |

number of elements in some classes $i$. To minimize the former perturbation effects, new global $C(\lambda)$ coefficients have been computed without any class separation. Then, imposing $C(\lambda)$ constant for all classes $i$, new exponential fits have been computed to get the intercepts $\bar{Q}_{90}(\lambda,i)$. The coefficients $\bar{C}(\lambda)$ and $\bar{Q}(\lambda,i)$ are also given in Table 6. The latter values show a slight increase with respect to those computed with class-dependent $C(\lambda,i)$.

The overall dependence of $\bar{Q}_{90}(\lambda,i)$ on $\lambda$ reflects the spectral dependence of the average $Q_n(\lambda)$ given in Table 4 with

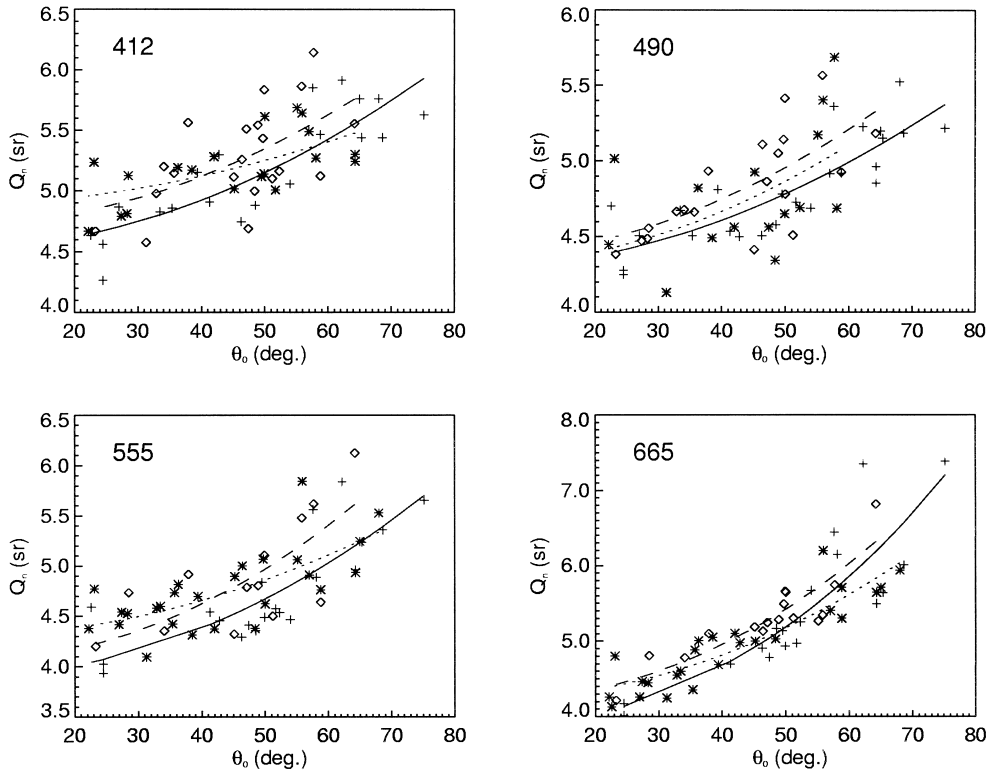


Fig. 5. $Q_n$($\lambda$,$i$) plotted as a function of $\theta_0$ for the three classes $i$ defined by $\varpi$($\lambda$,$i$) values, with the associated exponential fitting curves at 412, 490, 555, and 665 nm. + and solid lines, class 1; * and dotted lines, class 2; ◇ and dashed lines: class 3.

a decrease from 412 to 490–510 nm, followed by an increase toward 665 nm. At each $\lambda$, $Q_{90}(\lambda,i)$ show a general increase with $K_d(\lambda,i)$ values. $C(\lambda)$ data show a weak spectral dependence in the 412–510 nm region with an average of ~0.3 and increasing values of 0.38 and 0.74 at 555 and 665 nm, respectively. This is in general agreement with the trend of curves displayed in Morel and Gentili (1996) for $Q_n(\lambda)$ versus $\theta_0$ simulations. $Q_{90}(\lambda,i)$ and $C(\lambda)$ given in Table 6 at 490 nm for the first class $i$ [i.e., the class defined by the smallest $K_d(\lambda)$ values] have been intercompared with those proposed by Siegel (1984) and Aas and Hojerslev (1999) in the same spectral region for oceanic water. $Q_{90}(\lambda,i)$ show very close values (i.e., ~5.3 sr), whereas $C(\lambda)$ indicates a less pronounced dependence on $\theta_0$ (i.e., ~0.27 v.s. ~0.5 in Siegel 1984 and ~0.45 in Aas and Hojerslev 1999).

## Discussion

$Q_n(\lambda)$ *dependence on* $\theta_0$—As an alternative to the empirical exponential fitting function defined by Eq. 2, the following functions have also been investigated:

$$Q_n(\lambda) = Q_{90}(\lambda) + C(\lambda)\cos\theta_0 \quad (5)$$

and

$$Q_n(\lambda) = Q_{90}(\lambda) + C(\lambda)(\cos\theta_0)^{-2}. \quad (6)$$

Equation 5 was proposed by Aas and Hojerslev (1999), whereas Eq. 6 has a foundation in radiative transfer theory as $Q_n(\lambda) \sim R(\lambda)K_d(\lambda)/b_b(\lambda)$ (Gordon et al. 1988), and both $K_d(\lambda)$ and $R(\lambda)$ are proportional to $1/\cos\theta_0$ (Gordon 1994).

The fitting capabilities of Eqs. 2, 5, and 6 have been tested by use of $Q_n(\lambda)$ data at 665 nm (without any class separation) for which the dependence on seawater optical components other than pure seawater is weaker than that at shorter wavelengths. Results from the intercomparison, based on the analysis of determination coefficients $R^2$ and on root-mean square of differences (RMSd) show that:

(1) The fitting functions defined by Eqs. 2 and 5 perform similarly (i.e., $R^2 = 0.73$ for Eq. 2, $R^2 = 0.72$ for Eq. 5, and RMSd = 0.47 for both) even though, from the visual inspection of plots (not shown here), Eq. 2 performs slightly better than Eq. 5 in fitting $Q_n(665)$ data at $\theta_0 > 60°$; and

(2) The fitting function defined by Eq. 6 exhibits the worst results (i.e., $R^2 = 0.62$ and RMSd = 0.56), even though the visual inspection of plots (not shown here) highlights qualitatively good capabilities in fitting $Q_n(665)$ data at $\theta_0 > 60°$.

$Q_n(\lambda)$ *dependence on inherent optical properties*—The increase of $Q_{90}(\lambda,i)$ with $K_d(\lambda,i)$ at each $\lambda$ (*see Table 6*) show a corresponding slight increase in the average values of $a(\lambda,i)$, $b(\lambda,i)$, and $\varpi(\lambda,i)$ [e.g., $\varpi(\lambda,i)$ showing variations from 0.85 to 0.89 at 490 nm]. This suggests a dependence of $Q_n(\lambda)$ on the inherent optical properties, as already has been assessed by Morel and Gentili (1993) for oceanic water.

The use of $a(\lambda)$, $b(\lambda)$, and $\varpi(\lambda)$ (from AC-9 measurements) has been investigated as an alternative to $K_d(\lambda)$. The analysis, restricted to a fewer number of $Q_n(\lambda)$ elements because of the nonavailability of AC-9 data during the first year of CoASTS measurements, has shown the weaker capability of $a(\lambda)$, $b(\lambda)$, and $\varpi(\lambda)$, with respect to $K_d(\lambda,i)$, in discriminating the different classes of $Q_n(\lambda,i)$. The latter finding is highlighted by the intercomparison of Figs. 4 and 5 for $K_d(\lambda,i)$ and $\varpi(\lambda,i)$, respectively. Table 7 shows values of $Q_{90}(\lambda,i)$ and $C(\lambda,i)$ with the 90% confidence intervals and of the percentage difference (PD) resulting from the fits of $Q_n(\lambda,i)$ versus $\theta_0$ as defined by $\varpi(\lambda,i)$ values. The comparison of data in Table 7 with those given in Table 6 for $Q_n(\lambda,i)$ defined by $K_d(\lambda,i)$ values clearly highlights that:

(1) $Q_{90}(\lambda,i)$ does not orderly increase with $\varpi(\lambda,i)$, as is differently shown with $K_d(\lambda,i)$; and

(2) values of $Q_{90}(\lambda,i)$, 90% confidence intervals, and PD are generally larger than those observed with $K_d(\lambda,i)$.

*Model inversion*—In agreement with the former results, defining classes of $Q_n(\lambda,i)$ by use of $K_d(\lambda,i)$, the equation for a modeled $\tilde{Q}_n(\lambda,i)$ can be written as

$$\tilde{Q}_n(\lambda,i) = A_0(\lambda) + S(\lambda)\{\bar{Q}_{90}(\lambda_0,i)\exp[-\bar{C}(\lambda_0)\cos\theta_0]\} \quad (7)$$

where the values of $A_0(\lambda)$ and $S(\lambda)$ are given in Table 5 (with $A_0 = 0$ and $S = 1$ for $\lambda_0$), and the values of $Q_{90}(\lambda_0,i)$ and $C(\lambda_0)$ are given in Table 6 together with the $K_d(\lambda_0,i)$ interval limits for each of the three classes $i$ considered in the study.

Figure 6 shows scatter plots of $\tilde{Q}_n(\lambda,i)$ modeled with Eq. 7 and $\lambda_0 = 490$ nm, versus the measured $Q_n(\lambda,i)$. The RMSd given at each $\lambda$ to quantify the model intrinsic accuracy, shows the lowest agreement at 665 nm, mostly because of the poor correlation between $Q_n(665)$ and $Q_n(490)$ highlighted in Table 5. Scatter plots indicate some underestimate of the highest values of the modeled $\tilde{Q}_n(\lambda,i)$ with respect to the experimental $Q_n(\lambda,i)$. The former underestimate is probably induced by a general increase in the scattering of $Q_n(\lambda,i)$ on $\theta_0$ increase. This reduces the capability of Eq. 4 to fit the high $Q_n(\lambda,i)$ values [as, for instance, shown in Fig. 4 by $Q_n(665,i) > 7$ sr].

A reanalysis of the $Q_n(\lambda)$ data set by modeling $\tilde{Q}_n(\lambda,i)$ as a function of $\theta_0$ and $\lambda_0$ only—that is, neglecting any classification—has shown an appreciable increase of ~0.07 (on the average) in the RMSd at all $\lambda$, with the exception of $\lambda = 665$ nm (which showed no appreciable change). The scatter plots (not shown here) of the modeled $\tilde{Q}_n(\lambda)$ versus the measured $Q_n(\lambda)$ have displayed the most significant increase in differences, compared with the data shown in Fig. 6, for the small and the large $Q_n(\lambda)$ values at almost all wavelengths.

## Conclusions

The $Q_n(\lambda)$ data set analyzed in this work is of unique value because of the different conditions that characterized the measurements (i.e., variability in water types and a wide range of $\theta_0$). The analysis of the time series indicates the possibility of modeling $Q_n(\lambda)$ with a simple parametric model as a function of $\theta_0$ and $K_d(\lambda_0)$ at the reference wavelength $\lambda_0 = 490$ nm.

The parametric model could (1) ensure the integration of existing data sets lacking $Q_n$ data, (2) contribute to the validation of theoretical models of radiance distribution in seawater [even though only $Q_n(\lambda)$ values can be compared], and (3) support ocean color data processing when coupled with theoretical models.

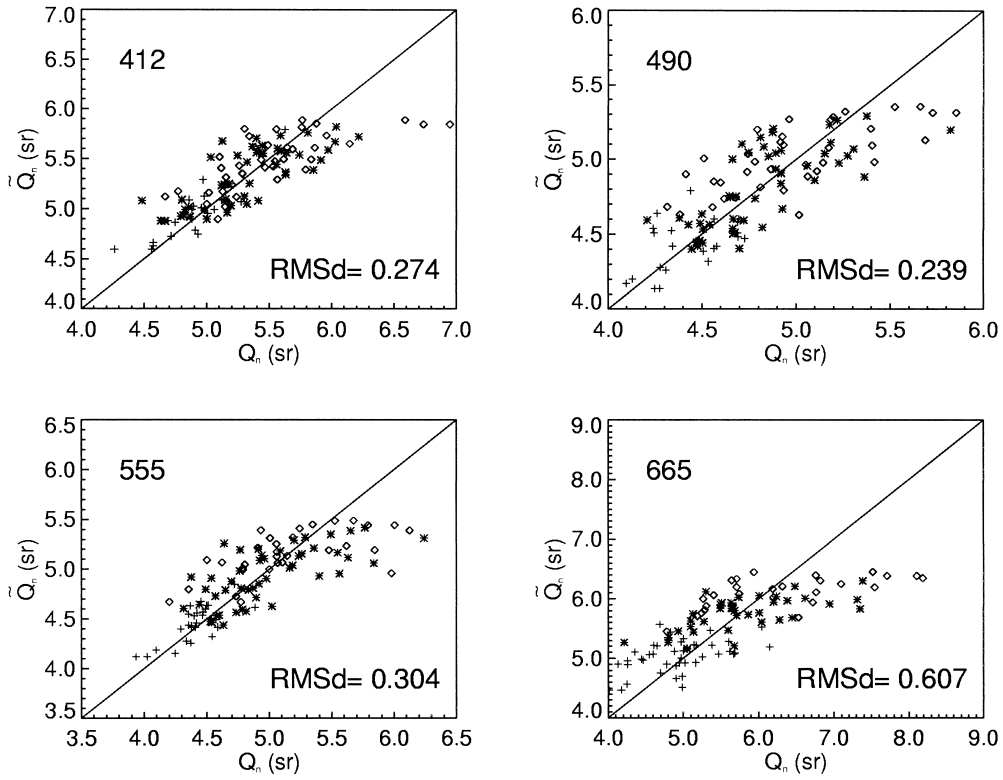


Fig. 6. Modeled $\tilde{Q}_n(\lambda,i)$ vs. measured $Q_n(\lambda,i)$ at 412, 490, 555, and 665 nm. Solid lines show the 1 : 1 ratio. +, class 1; *, class 2; and ◇, class 3.

Limits of the proposed parametric model are the relatively small number of data and the restricted geographic region in which the measurements have been collected (i.e., the North Adriatic Sea), which does not ensure any a priori extendibility to other geographic areas. Further work should be addressed to the analysis of $Q_n(\lambda)$ sample data, through radiative transfer modeling of $L_u(\lambda,z)$ and $E_u(\lambda,z)$. Such an activity, supported by the availability of atmospheric and marine inherent optical properties measured at the same time of the $L_u(\lambda,z)$ and $E_u(\lambda,z)$ profiles, should assess accuracy of $Q_n(\lambda)$ modeling for coastal waters.

## *References*


AAS, E., AND N. K. HØJERSLEV. 1999. Analysis of underwater radiance observations: Apparent optical properties and analytic functions describing the angular radiance distribution. J. Geophys. Res. **104:** 8015–8024.

AUSTIN, R. W. 1979. Coastal Zone Color Scanner radiometry, p. 170–177. *In* Ocean Optics VI. Proceedings, Soc. Photo-Optical Instrument. Eng. (SPIE), v. 208.

BERTHON, J. F., G. ZIBORDI, AND S. B. HOOKER. 2000. Marine optical measurements of a mucilage event on the northern Adriatic Sea. Limnol. Oceanogr. **45:** 322–327.

BUITEVELD, H., J. H. HAKWOORT, AND M. DONZE. 1994. The optical properties of pure water, p. 174–183. *In* J. S. Jaffe [ed.], Ocean Optics XII, Proceedings Soc. Photo-Optical Instrument. Eng. (SPIE), v. 2258.

DOYLE, J. P., AND G. ZIBORDI. 1998. Correction of oceanographic tower-shading effects on in water optical measurements. Proceedings in Ocean Optics XIV, Kailua-Kona, November 10–13, 1998.

FERRARI, G. M., M. D. DOWELL, S. GROSSI, AND C. TARGA. 1996. Relationship between the optical properties of chromophoric dissolved organic matter and total concentration of dissolved organic carbon in the southern Baltic Sea region. Mar. Chem. **55:** 299–316.

GORDON, H. R. 1994. Modeling and simulating radiative transfer in the ocean, p. 3–41. *In* R. W. Sinrad, K. L. Carder, and M. J. Perry [eds.], Ocean optics. Oxford Univ. Press.

———, O. B. BROWN, R. H. EVANS, J. W. BROWN, R. C. SMITH, K. S. BAKER, AND D. K. CLARK. 1988. A semianalytic radiance model of ocean color. J. Geophys. Res. **93:** 10,909–10,924.

———, AND K. DING. 1992. Self-shading of in-water optical measurements. Limnol. Oceanogr. **37:** 491–500.

KIRK, J. T. O. 1994. Estimation of the absorption and the scattering coefficients of natural waters by use of underwater irradiance measurements. Appl. Optics **33:** 3276–3278.

LOISEL, H., AND A. MOREL. 1998. Light scattering and chlorophyll concentration in case 1 waters: A reexamination. Limnol. Oceanogr. **43:** 847–858.

MARITORENA, S., A. MOREL, AND B. GENTILI. 1994. Diffuse reflectance of oceanic shallow water: Influence of water depth and bottom albedo. Limnol. Oceanogr. **39:** 1689–1703.

MOREL, A., AND B. GENTILI. 1991. Diffuse reflectance of oceanic waters: Its dependence on sun angle as influenced by the molecular scattering distribution. Appl. Optics **30:** 4427–4438.

———, AND ———. 1993. Diffuse reflectance of oceanic waters, II, bidirectional aspects. Appl. Optics **32:** 6864–6879.

———, AND ———. 1996. Diffuse reflectance of oceanic waters, III, implications of bidirectionality for the remote-sensing problem. Appl. Optics **35:** 4850–4862.

———, K. J. VOSS, AND B. GENTILI. 1995. Bidirectional reflectance of oceanic waters: A comparison of modeled and measured upward radiance fields. J. Geophys. Res. **100:** 13,143–13,150.

MUELLER, J. L. 1995. Comparison of irradiance immersion coefficients for several marine environmental radiometers (MERs), p. 3–15. *In* S. Hooker, E. Firestone, and J. Acker [eds.], Case studies for SeaWiFS calibration and validation, part 3. SeaWiFS Technical Report Series, NASA TM 104566, v. 27, NASA Goddard Space Flight Center.

———, AND R. W. AUSTIN. 1995. Ocean optics protocols for SeaWiFS validation, revision 1. SeaWiFS Technical Report Series, NASA TM104566, vol. 25, S. B. Hooker and E. R. Firestone [eds.], NASA Goddard Space Flight Center, Greenbelt, Maryland, 66 p.

PETZOLD, T. J., AND R. W. AUSTIN. 1988. Characterization of MER-1032. Technical Memorandum EV-001-88t, Visibility Laboratory. Scripps Institution of Oceanography.

POPE, R. M., AND E. S. FRY. 1997. Absorption spectrum (380–700 nm) of pure water. II. Integrating cavity measurements. Appl. Optics **36:** 8710–8723.

SIEGEL, H. 1984. Some remarks on the ratio between the upward irradiance and nadir radiance just beneath the sea surface. Beiträge zur Meereskunde **51:** 75.

TASSAN, S., AND G. M. FERRARI. 1995. An alternative approach to absorption measurements of aquatic particles retained on filters. Limnol. Oceanogr. **40:** 1358–1368.

TYLER, J. E. 1960. Radiance distribution as a function of depth in a underwater environment. Bull. Scripps Inst. Oceanogr. Univ. Calif. **7:** 363–412.

WETLABS. 2000. AC-9 protocol (rev. B). Western Environmental Technology Laboratories, Inc., 620 Apple-gate, Philomath, Oregon.

ZANEVELD, J. R., J. C. KITCHEN, AND C. MOORE. 1994. The scattering error coefficient of reflective absorption measurements, 44–54. *In* Ocean Optics XII. Proc. Soc. Photo-Optical Instrum. Eng. (SPIE), v. 2258.

ZIBORDI, G., J. P. DOYLE, AND S. HOOKER. 1999. Offshore tower shading effects on in-water optical measurements. J. Atmos. Ocean. Technol. **16:** 1767–1779.

———, AND G. M. FERRARI. 1995. Instrument self shading in underwater optical measurements: Experimental data. Appl. Optics **34:** 2750–2754.

*Received: 17 May 2000*
*Accepted: 19 February 2001*
*Amended: 9 March 2001*